



Fabrication of sacrificial wax pattern through large-scale fused granulated fabrication (FGF-AM) hybrid manufacturing system

Piyush Arora¹ · Shirin Dehgahi¹ · Sajid Ullah Butt¹ · David S. Nobes² · Ahmed Jawad Qureshi¹

Received: 21 February 2024 / Accepted: 25 June 2024
© The Author(s), under exclusive licence to Springer Nature Switzerland AG 2024

Abstract

Direct rapid investment casting integrates additive manufacturing (AM) technology into conventional investment casting. This approach addresses the challenge of high lead time and cost but is effective only on a small scale. It utilizes thermoplastics such as ABS as a sacrificial pattern material, but after burnout, thermoplastics can lead to defects such as shell cracking and residual ash. This study uses large-scale extrusion AM technology, fused granulated fabrication (FGF-AM), to address these challenges. This approach involves printing sacrificial patterns using wax, a preferred foundry material. This novel technique can produce highly scalable objects due to its superior extrusion rate. The design of experiments is used to optimize the crucial printing parameters. In-situ CNC machining was incorporated to mitigate stair-stepping defects resulting from layer-by-layer printing and to improve surface quality and dimensional precision, ensuring compliance with investment casting (IC) standards. Tensile testing was conducted per ISO standards at different sections to assess the variations in mechanical properties along the print volume. Finally, to demonstrate the capability of the in-house hybrid manufacturing system, a case study was performed by fabricating an ASME wax slip-on flange. The developed system achieved 10–20 times higher productivity than alternative 3D printing methods, which shows its potential for industrial scalability.

Keywords In-situ hybrid manufacturing system · Hybrid investment casting · Design of experiments · Large-scale additive manufacturing · Dimensional tolerance

1 Introduction

Investment casting (IC) has gained significant prominence due to its capacity to produce intricate, near-net, and geometrically complex metallic components at an industrial scale. Industries such as automotive, aerospace, defense, power, oil and gas, food processing, and customized commercial products, such as medical implants, have substantially relied on IC processes [1, 2]. As of 2022, the global market share for IC surpassed a valuation of US\$16 billion and is projected to exceed the US\$20 billion threshold by 2028 [3].

1.1 Limitations of conventional IC process

The IC framework unfolds as a sequential operation, with the most prominent bottleneck in the initial stage being master mold production. This process relies on the complex tooling of metals, such as aluminum. As depicted in Fig. 1, the conventional IC methodology entails significant costs ranging from tens to hundreds of thousands of dollars based on size and complexity. In addition, it may demand an extensive time of up to 21 weeks, with mold production alone accounting for almost 70% of the total time [4]. Consequently, the economic viability of the IC process is most evident in large-batch production scenarios [4, 5]. Furthermore, any deviations or adaptations to the sacrificial pattern in use, mandate the creation of an entirely new master mold, causing inevitable capital outlays and delays in the production process [6, 7].

✉ Ahmed Jawad Qureshi
ajquresh@ualberta.ca

¹ ADaMS Lab, Department of Mechanical Engineering, University of Alberta, Edmonton, AB T6G 1H9, Canada

² Department of Mechanical Engineering, University of Alberta, Edmonton, AB T6G 1H9, Canada

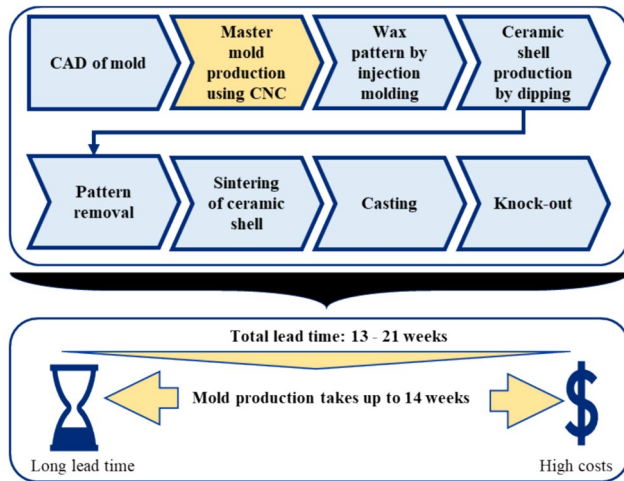


Fig. 1 Limitations in the conventional investment casting process

1.2 Rapid investment casting (RIC)

Acknowledging the challenges in IC, Cheah et al. [4] introduced various manufacturing chains integrating additive manufacturing (AM) technologies to reduce lead times and costs. AM, or 3D printing, involves creating three-dimensional objects through the successive layered deposition of material [8]. AM offers significant potential to improve material productivity and reduce environmental impacts compared to conventional methods, promoting sustainable development (SDG-12: Responsible consumption and production) and cost-effective manufacturing approach [9]. The infusion of AM techniques within the conventional IC framework is designated as rapid investment casting (RIC) [2] or hybrid investment casting (HIC) [6]. In a comparative study, Lee et al. [10] revealed a substantial 89% reduction in time and a 60% reduction in costs for pattern fabrication achieved through the FDM process.

In the literature, various 3D printing methodologies, such as stereolithography, SLS, and FDM, have been used to produce sacrificial patterns [2, 4]. The material

compositions, resulting attributes, and need for any pre/post-processing steps for the standard AM techniques for IC are outlined in Table 1. It is observed that SLA and FDM emerge as the most favored options due to their accessibility in achieving high-quality and cost-effective patterns [2].

1.3 Limitations of rapid investment casting

The AM techniques in Table 1 present inherent limitations in industrial-scale deployment. A primary constraint restricting the scalability of casting dimensions is the limited range of printing layer heights (25–300 microns). Moreover, specific AM methodologies involve intricacies and cost implications. For instance, SLA-AM involves post-processing steps impacting cycle time, RFP and SLS need controlled environmental conditions leading to elevated energy consumption, and SLA and SLS techniques require specialized equipment, such as laser and intricate design considerations, incurring substantial capital investment [2]. Current AM technique limitations highlight the need for an innovative, cost-effective, and simplified large-scale additive manufacturing solution.

The IC process is used extensively for its precision castings that rely on high-quality sacrificial patterns. Industry standards require specific criteria for surface quality (16–20 $\mu\text{m Ra}$) and dimension (± 0.05 to ± 0.254 mm) [10]. However, patterns printed through standard AM techniques have lower surface quality and dimensional accuracy [17]. Besides that, researchers encounter a significant challenge of shell cracking during the pattern removal phase [18]. Thermoplastics used in 3D printing possess a high coefficient of thermal expansion (CTE), which induces thermal stresses during pattern burnout, potentially causing cracking if these stresses exceed the shell's modulus of rupture [19]. Due to its distinct advantages, including substantially lower CTE and complete burnout during casting, wax is the most preferred pattern material for IC [20]. However, some AM techniques for direct RIC applications cannot directly use

Table 1 AM techniques implemented in the direct RIC process

AM technique	Material	Layer height (μm)	Dimensional tolerance (mm)	Surface roughness (μm)	Residual ash (%)	Additional pre/post-processing
SLA [1]	Castable wax	25	0.05	–	0.1	Post-curing
FDM [11]	ABS	100–200	0.971	0.3	–	Chemical treatment
MJP [12]	Acrylate	25	0.4	3.89	–	N.A
RFP [13, 14]	Water/ice	150	0.94	3.2	–	N.A
Binder jetting [15]	PMMA powder	300	0.43	28	–	Wax and epoxy infiltration
SLS [16]	Castform Powder	150	–	3	0.02	Wax infiltration

wax due to constraints related to its physical state, type, and the printer's layer-building mechanisms. These limitations necessitate the exploration of innovative solutions to enhance RIC processes.

1.4 Innovative solutions for limitations of RIC

Fused granulated fabrication (FGF-AM) is a large-scale extrusion-based AM technology that addresses scalability issues and could be ideal for RIC applications due to its simple printing mechanism. It uses pellets instead of filament [21] that are fed and moved into the barrel through a rotating screw while heated through external heaters ensuring pellets melt. The extrudate is deposited through a nozzle onto a heated bed at a controlled viscosity. FGF-AM can produce large-scale components, up to 7m³, emphasizing its industrial utility [22].

With scalability, the issues of poor surface quality and dimensional precision get worse. One of the proposed solutions is to reduce the layer height [23], but this would significantly extend printing time. An alternative approach involves vapor bath smoothing of FDM-fabricated ABS patterns, significantly reducing surface roughness (from 14.40 μm to 0.37 μm) [11]. Another approach is to enhance the surface finish by creating a hybrid manufacturing framework that combines subtractive manufacturing with the existing additive module, such as proposed by Amanullah et al. [24], who integrated abrasive milling operations with a desktop FDM printer. Their research shows a significant improvement, with up to 99% enhancement in dimensional accuracy and 91.3% in surface roughness (Ra) for machined PLA specimens. FGF is suitable for printing large-scale parts, and integrating subtractive modules could be used to improve the lower dimensional accuracy and surface quality, which is an unexplored area.

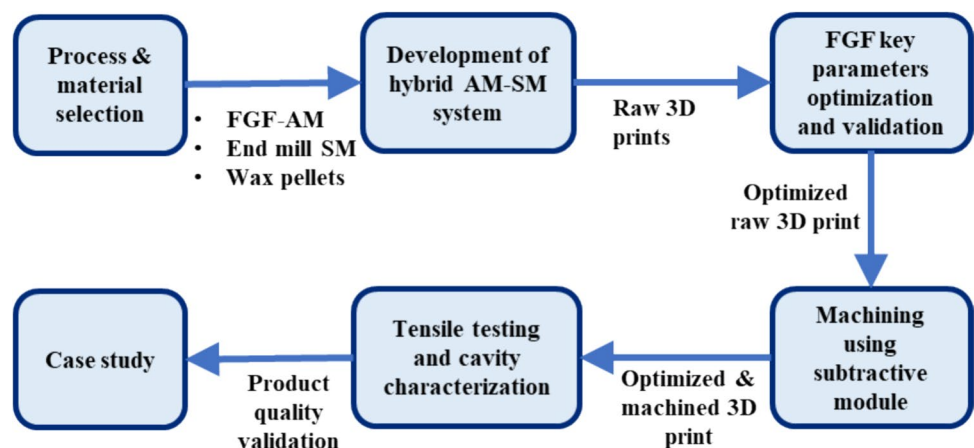
1.5 Research objective

This study aims to overcome the constraints associated with traditional and rapid investment casting methods by employing large-scale extrusion-based fused granulated fabrication (FGF-AM) technology for producing sacrificial patterns with wax, thereby addressing issues related to shell cracking. The large-scale hybrid investment casting process would enable the production of larger components across industries. In aerospace, it can manufacture turbine blades and structural components up to a meter in length. In automotive, it can be utilized for engine components like cylinder heads and crankshafts. In addition, it finds applications in the energy sector for pump impellers and in medical implants for knee and hip replacements [25]. The key printing process parameters underwent optimization and validation through the design of experiments (DoE) to ensure the structural integrity of the pattern. An in-situ CNC machining facility was incorporated to enhance the printed pattern's surface quality and dimensional precision according to IC standards. Tensile testing was conducted at different sections to validate the uniformity of the mechanical properties along the print volumes. Finally, cavity analysis was performed on wax specimens to ensure the machine could produce artifacts with near-zero porosity.

2 Methodology

The methodology, outlined in Fig. 2 and elaborated in subsequent sections, commences with selecting suitable additive and subtractive modules and wax pellets. It is followed by the development of a large-scale hybrid manufacturing system for experimental purposes. Critical printing parameters are then optimized and validated to minimize post-processing. The optimized specimens undergo machining using a subtractive module, and measurements are taken to assess the achieved surface finish and dimensional tolerance,

Fig. 2 Flow chart of the followed methodology



ensuring compliance with investment casting (IC) standards. Tensile testing is conducted on various sections of wax specimens produced by the hybrid system to confirm the uniformity in mechanical properties. Subsequently, cavity characterization is performed to verify the system's capability to create components with minimal porosity. Finally, a case study validates the system's proficiency in fabricating products suitable for industrial applications.

2.1 Fused granulated fabrication (FGF-AM) technology

The current study utilizes an SJ-35 Desket-H pellet-fed single-screw extruder developed by Robotdigg in China [26]. The print head schematic and the overall dimensions are

shown in Fig. 3. This extruder can print with a 2kg/h. mass flow rate.

2.2 Hybrid manufacturing system (HMS)

Figure 4 shows an in-house advanced Cartesian gantry-based hybrid manufacturing system with a print volume exceeding one cubic meter. Driven by Nema-34 stepper motors and guided by precision linear actuators, the gantry supports a maximum vertical payload of 50 kg with a precision of 20 microns. It has a square-shaped heated aluminum print bed capable of maintaining temperatures up to 200 °C. The system also features a subtractive module a 500-W air-cooled CNC spindle to mitigate surface defects.

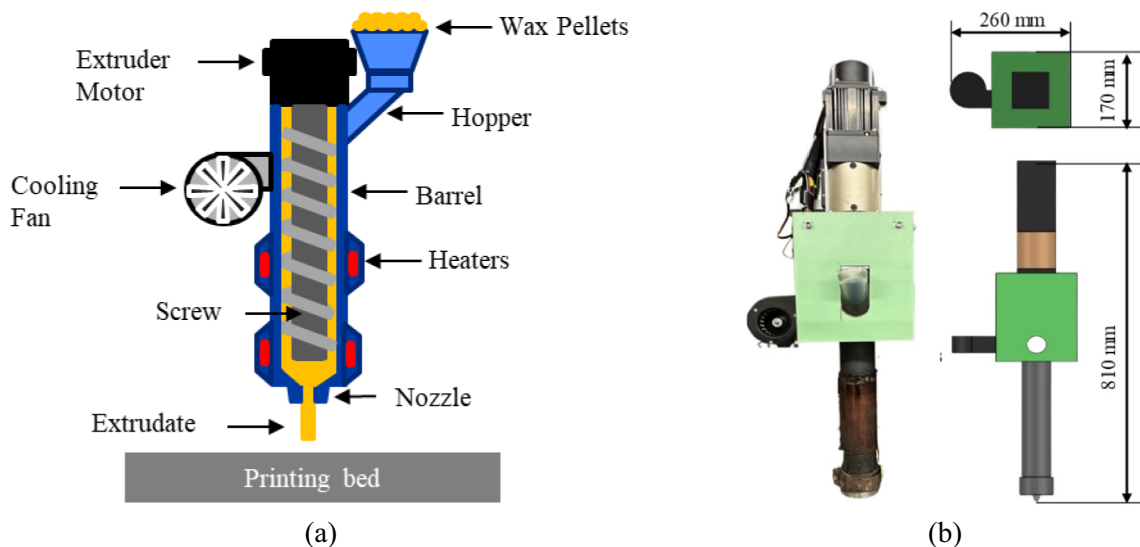


Fig. 3 **a** Schematic of pellet-fed print head's components, and **b** SJ-35 extruder overall dimensions

Fig. 4 In-house designed and developed hybrid manufacturing system

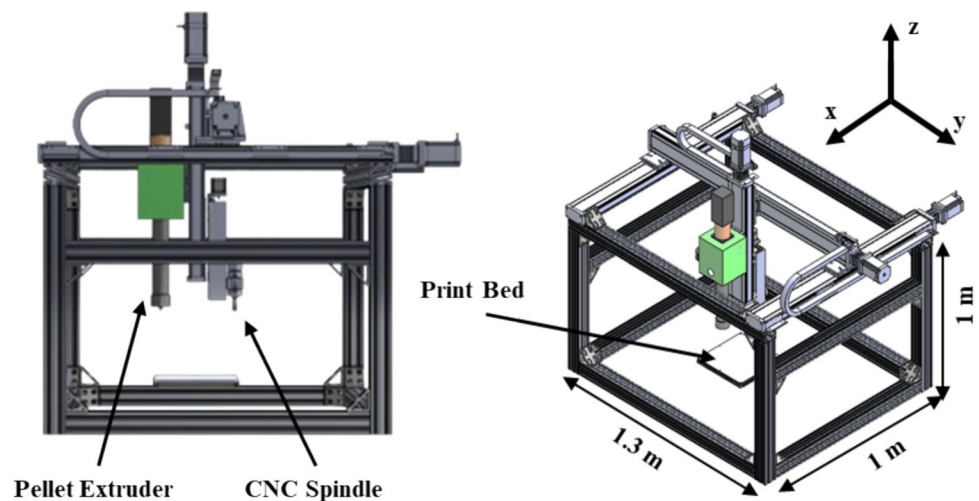
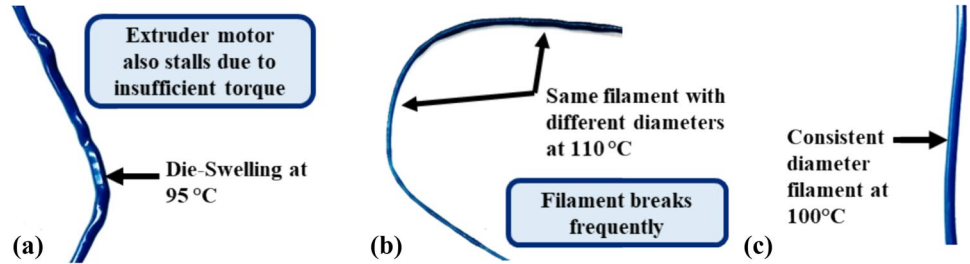


Table 2 Segregation of influential printing parameters for FGF-AM used in this study

Fixed variables (FVs)	Independent variables (IVs)	Dependent variables (DVs)
Type and shape of raw material	Extruder motor speed, ω (RPM)	Mass flow rate, M (kg/h)
Bed temperature (90 °C)	Nozzle size, d (mm)	Extrusion velocity, V_e (mm/s)
Barrel temperature (100 °C)	Layer height, h (mm)	Scanning velocity, V_{xy} (mm/s)
	Overlap percent, p (%)	Bead width, b (mm)

Fig. 5 a Die-swelling due to high viscosity at 95 °C, b inconsistent extrudate due to low viscosity at 110 °C, and c consistent extrudate at 100 °C



2.3 Pellets material

This project utilizes proprietary Print-2-Cast (P2C) wax pellets provided by Machinable Wax, USA [27]. In contrast to thermoplastics, which release harmful constituents during burnout, wax promotes environmental sustainability and is reusable. Each P2C pellet has a cylindrical geometry with a uniform diameter and height of 3 mm. The wax has a precise melting temperature of 117 °C and a specific density (ρ) of 912.38 kg/m³, aligning with the experimental objectives of this research.

2.4 FGF-AM key process parameters

To achieve reliable printability, AM techniques rely on optimizing critical factors such as shape retention, inter-layer bonding, bed adhesion, etc. This involves careful examination and adjustment of independent variables (IV), stabilization of fixed variables (FV), and precise control of dependent variables (DV). Table 2 characterizes influential printing parameters into these groups.

The study establishes fixed variables guided by specific constraints. For example, the manufacturer determines the shape and size of the wax pellets, and the bed temperature is kept at 90 °C in adherence to the manufacturer's recommendations [27]. As illustrated in Fig. 5, a barrel temperature of 95 °C resulted in die swelling due to increased shear stress, whereas higher temperatures (~110 °C) caused inconsistent diameter and filament breaks owing to reduced viscosity. Optimal conditions, characterized by a consistent diameter and continuous flow, were observed at 100 °C, leading to the decision to set the barrel temperature at this value.

In this study, independent variables refer to parameters that remain unaffected by other factors and are altered to

observe their impact on dependent or response variables. The independent variables include Extruder motor speed (ω), adjusted within a range of 0–800 RPM, avoiding exceeding 80% of the motor capacity. The nozzle size (d) varies between 3 and 4 mm based on nominal sizes in the literature [21]. The layer height (h) is modified within the 2–2.8 mm range, maintaining proportionality to the nozzle size. Lastly, overlap percent (p) ranges from 0 to 4% of bead width to prevent inter-bead cavities.

The dependent variables in this study include the mass flow rate (M , kg/h) of the extrudate that relies on extruder motor speed (ω , RPM) (IV), nozzle size (d , mm) (IV), and barrel temperature (FV), and its measurement and use are presented in results sections. The second dependent variable is extrusion velocity (V_e , mm/s), which is determined by the mass flow rate (DV), nozzle size (IV), and the density of the material (ρ , kg/m³), as shown in the following equation:

$$V_e = \frac{\dot{M}}{9\pi d^2 \rho} \times 10^7 \tag{1}$$

Scanning velocity (V_{xy} , mm/s) (DV) is dependent upon layer heights (h , mm) (IV), nozzle size (IV), and extrusion

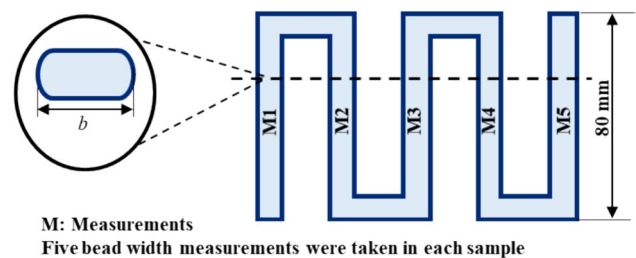


Fig. 6 Schematic of specimen printed for bead width measurements

Table 3 Influential printing parameters with their levels

Factor Type	Parameters	Level [- 1]	Level [0]	Level [+ 1]
Continuous	Extruder Motor speed (ω , RPM)	400	600	800
	Layer Height (h , mm)	2.0	2.4	2.8
	Overlap percent (p , %)	0	2	4
Categorical	Nozzle Size (d , mm)	Level [1]	Level [2]	
		3	4	

velocity (DV) as shown in 2 [28] and its calculations and use are shown in results sections:

$$V_{xy} = \frac{V_e}{\left(\frac{4h}{\pi d} + \left(\frac{h}{d}\right)^2\right)} \quad (2)$$

Bead width (b , mm) (DV) depends on independent variables: extruder motor speeds, nozzle sizes, and layer heights. In this study, bead width is measured for all possible combinations of independent variables using a Vernier caliper on a specimen, as shown in Fig. 6 and explained in the results section.

2.5 Design of experiments (DoE)

Four independent variables have been identified for this study. To achieve better dimensional tolerance and surface finish and to minimize the need for extensive

post-processing, i.e., machining, the selected parameters were optimized using the design of experiments for which the levels and the selected values of these parameters are shown in Table 3. The first three continuous parameters allow optimal values anywhere within the specified ranges. At the same time, nozzle size (d) is a categorical factor that yields discrete optimal values at the chosen levels. For this study, the objective is to reduce the response variables: stair-stepping depth and the presence of valleys and ridges [24], as shown in Fig. 7.

The selected specimen for DoE is a cuboid of 60 mm in length, with five adjacent beads in four layers, as shown in Fig. 8. Stair-stepping depth is measured from the sides while valleys and ridges from the top surface using the laser profilometer with a 2 μm resolution (PRO 2, SICK [29]). Multiple readings of both response variables were taken at various locations for each specimen to maintain statistical rigor. The central composite design (CCD) DoE approach was chosen as it yields higher-degree polynomial results



Fig. 7 Response variables selected for the DoE **a** stair-stepping depth and **b** valleys and ridges

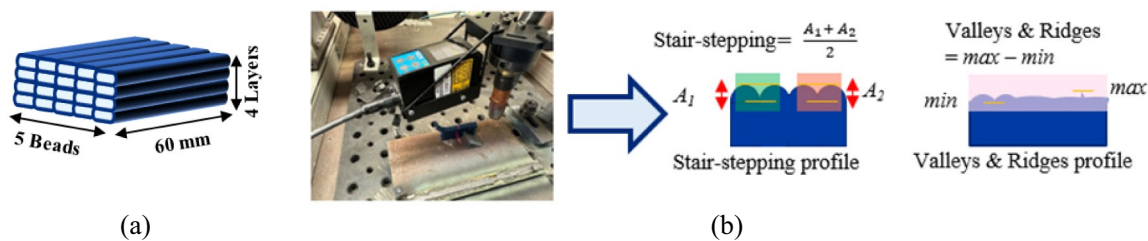


Fig. 8 (a) Specimen schematic and **b** data collection and acquisition using profilometer

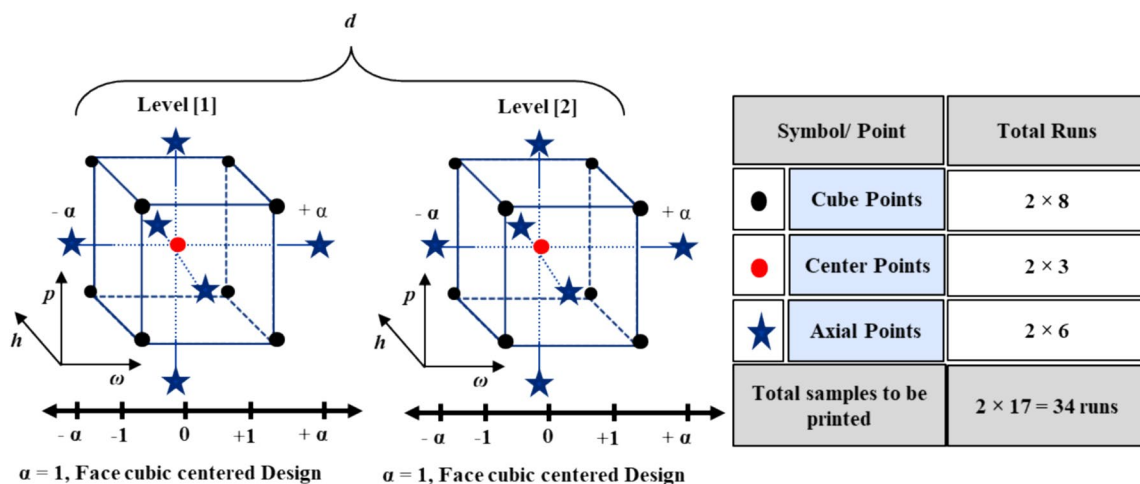


Fig. 9 CCD approach applied to the study and resulted experimental runs

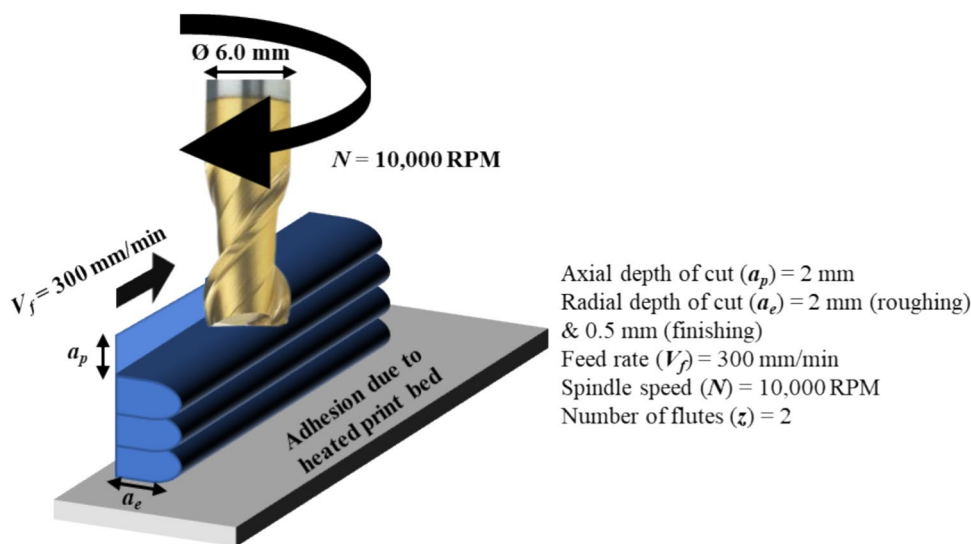
with fewer experimental runs than other DoE methodologies. Figure 9 illustrates the distribution of experimental runs using CCD: left cube shows 17 points of level [1] of d and right cube shows 17 points of level [2] of d , which resulted in 34 specimens being printed.

Both response variables were measured for each specimen and to assess the impact of each individual factor, Analysis of variance (ANOVA) [30] was performed on Minitab software [31]. Printing parameters were optimized using the response optimizer feature. Ultimately, the model was verified by printing multiple specimens using these optimal parameters, measuring their response variables, and comparing them with the Minitab’s output.

2.6 Surface roughness and dimensional tolerance measurements

Based on optimal parameters, multiple cuboidal specimens with 40. mm × 40. mm × 30. mm ($L \times W \times H$) were printed and machined into smaller cuboids (30. mm × 30. mm × 25. mm) using in-situ end-mill with the process parameters shown in Fig. 10. These specimens were tested for surface roughness and dimensional tolerance at various locations, and the results were compared with the IC standards. Dimensional measurements were made using a digital caliper with a 0.01 mm resolution and surface roughness was evaluated using a ZEISS CSM-700 confocal laser scanning microscope [32].

Fig. 10 CNC machining parameters used for post-processing the 3D printed wax workpiece



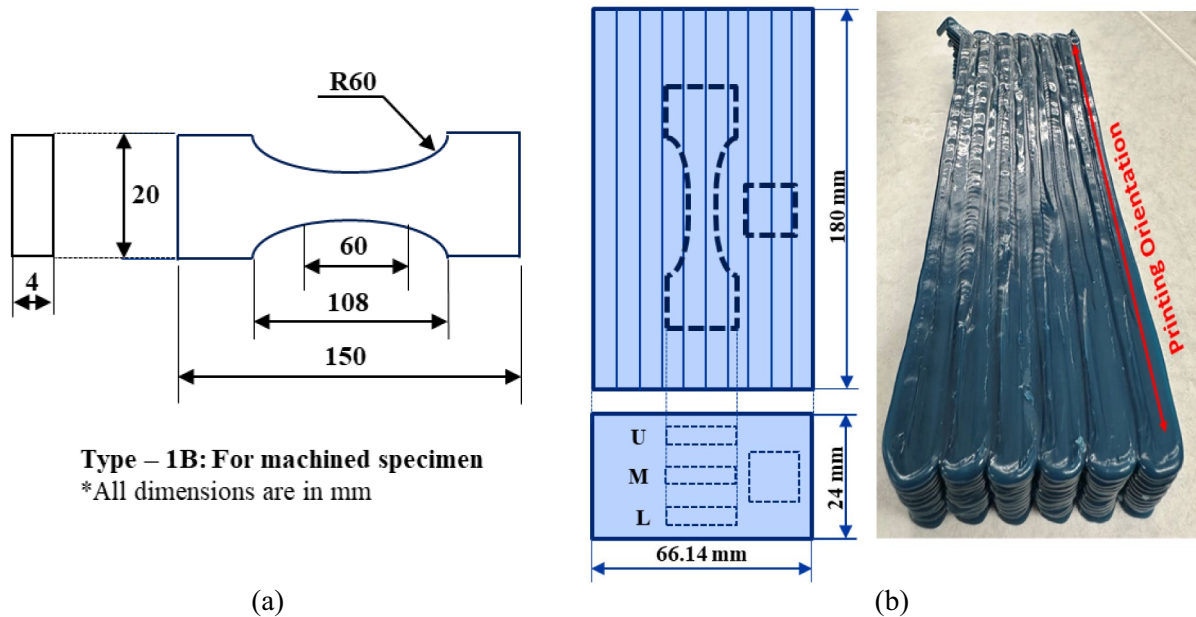


Fig. 11 a ISO 527–2 dog-bone dimensions and b procedure for specimen collection from the printed plate

2.7 Tensile testing and cavity characterization

For the tensile test, wax dog-bone specimens were produced following ISO 527–2 [33], as shown in Fig. 11a, using optimal parameters. Three plates were printed, and three specimens were machined from each plate at equidistant locations distributed vertically, as illustrated in Fig. 11b. This design aimed to explore the potential influence of sample location on the mechanical properties, considering layer dependent alterations in the wax material. The testing was performed on an Instron 3360 series UTS, USA [34], and the results were assessed. In addition, a 10 mm cube was machined from each plate to examine the presence of cavities due to inter-bead voids. The mass and volume of the cubes were measured, and the sample cubes' densities were compared to the material density.

3 Results and discussion

This section presents the results obtained from all the analyses mentioned in the previous sections.

3.1 Dependent variables characterization

For printing of the parts, the ratio of scanning and extrusion velocities is a parameter that influences the quality of the beads. Figure 12 gives the required scanning velocity based on the calculated extrusion velocity, which is further dependent upon the mass flow rate, again a dependent variable. For

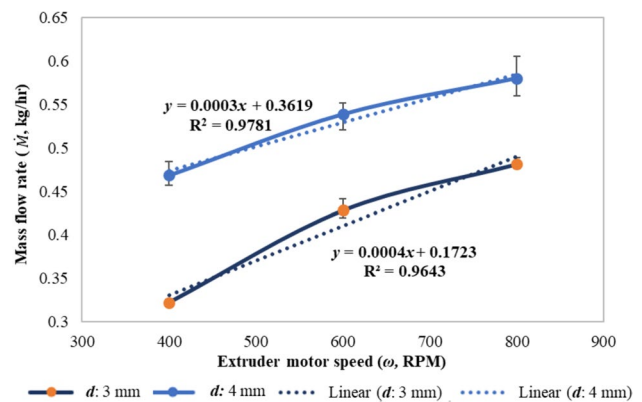


Fig. 12 Mass flow rate of the extrudate at different motor speed, nozzle sizes and 100 °C barrel temperature

better print quality, the required scanning velocity must be calculated for each combination of independent variables, and it starts with measuring the mass flow rate of the extrudate, which is measured for different RPM and nozzle sizes. For each data point, five measurements were performed for 10 s each to establish statistical control, which is presented in Fig. 12 with standard deviations. The results show a linear relationship between mass flow rate and extruder motor speed, indicating reliable results. A significant increase in flow rate is observed with an enlarged nozzle size from 3 to 4 mm, while a peak flow rate of approximately 0.6 kg/h was achieved at an extruder speed of 800 RPM with a 4 mm nozzle.

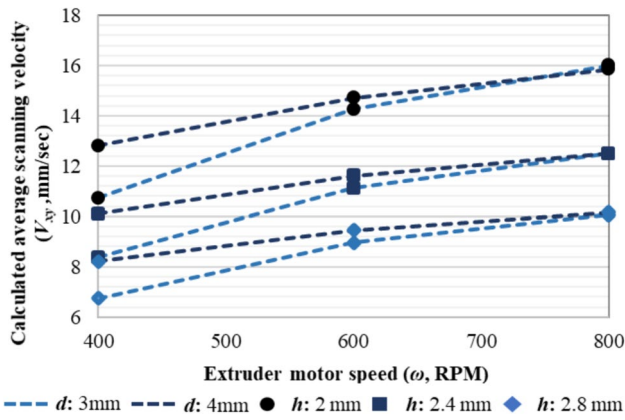


Fig. 13 Influence of prominent printing parameters on the scanning velocity

Scanning velocity was calculated using 1, 2, layer heights, and the measured mass flow rate at various combinations of extruder motor speed and nozzle sizes, as shown in Fig. 13. An upward trend in scanning velocity is observed with increasing layer height and extruder motor speed. The relationship with nozzle size shows distinct behavior, influencing at lower motor speed ranges but diminishing as it approaches higher levels, resulting in near-equivalent scanning velocities.

Once the respective scanning velocity for all the combinations of independent variables was known, bead width was measured for all possible combinations of independent variables and respective scanning velocity. The results are shown in Fig. 14. Increasing layer height for both nozzle

sizes led to wider bead widths, while elevating nozzle size under specific layer heights resulted in reduced bead width. Extruder motor speed, displaying distinctions in average values, showed insignificant differences due to a significant overlap of standard deviations. This trend results from applying the analytical equation for calculating scanning velocity, linked to extrusion velocity (increasing with higher extruder speed) and the h/d ratio. This approach mitigates the influence of extruder motor speed on bead width when the h/d ratio remains constant.

3.2 Optimization of independent variables

ANOVA was used to investigate the impact of each independent variable on the response variables, shown in Fig. 15, with the blue solid axis representing the stair-stepping depth and the black dashed axis valleys and ridges. Subplots for continuous factors, such as motor speed, reveal a linear relationship with valleys and ridges but a quadratic one with stair-stepping depth. The categorical factor, nozzle size, in the last subplot indicates a decrease in both responses with increased nozzle size, suggesting a preference for a 4 mm nozzle size. The model achieves high R-squared values, reaching 93.39% for stair-stepping depth and 94.25% for valleys and ridges, indicating a substantial attribution of variability to the investigated factors.

Figure 16 presents Pareto charts for both response variables, visually highlighting the most influential parameters based on the 80/20 rule. Figure 16a depicts a chart for stair-stepping depth, where layer height emerges as the most impactful parameter, contributing over 43%. It aligns with

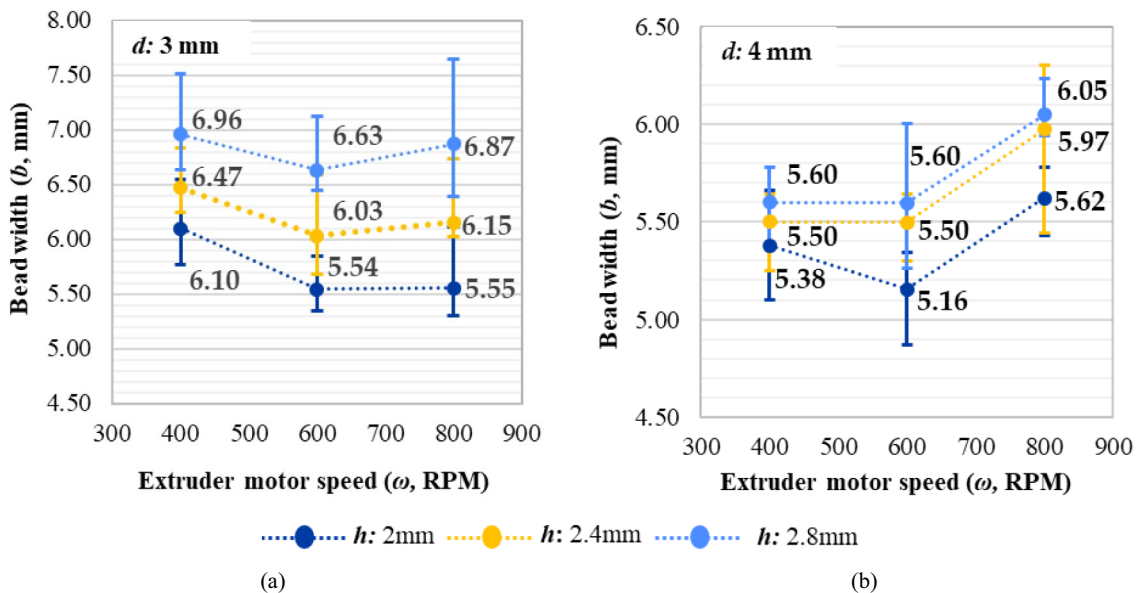


Fig. 14 Measured bead widths at pre-defined parameters with nozzle size a 3 mm and b 4 mm

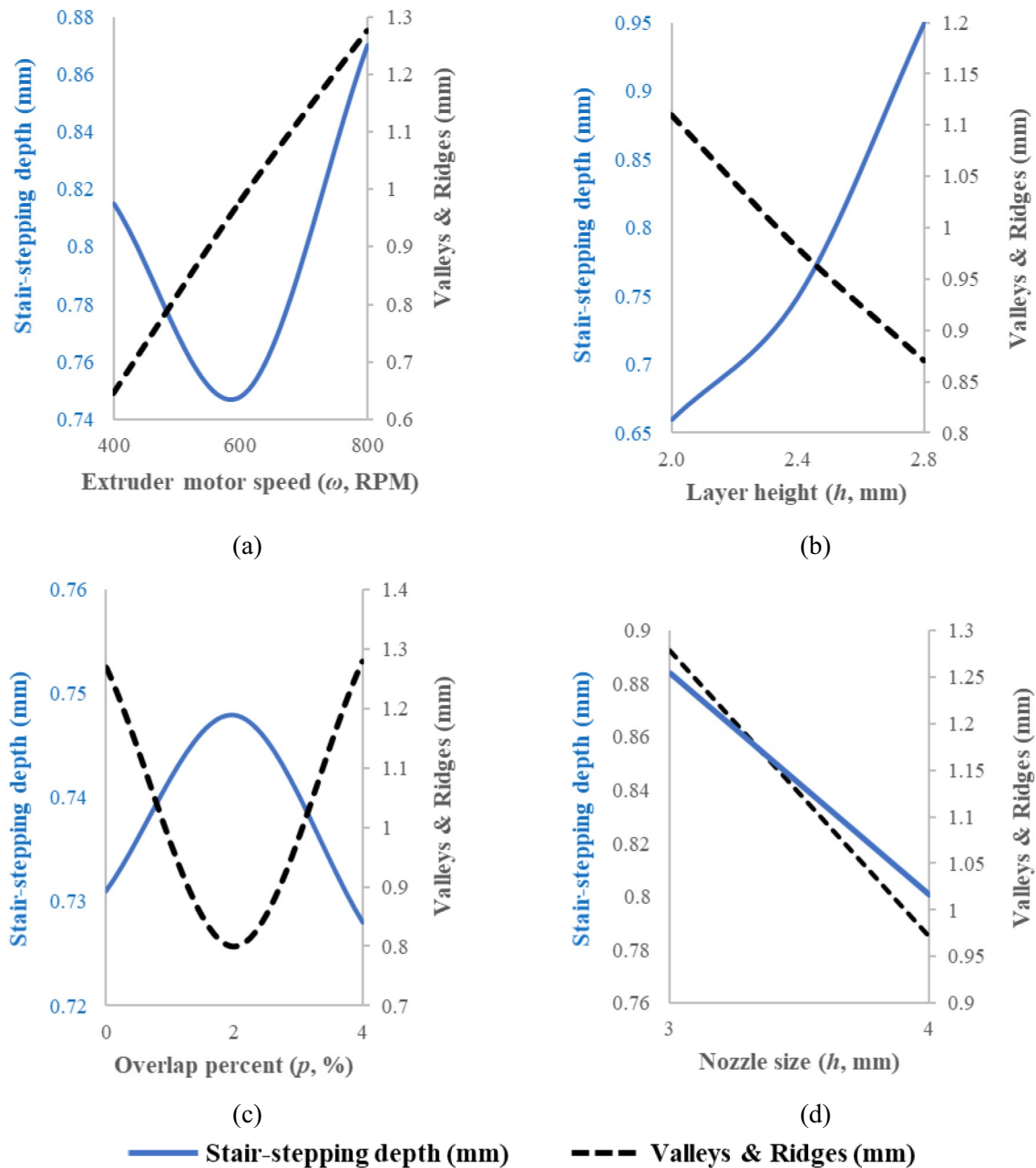


Fig. 15 Main effect plots for both the response variables with varying **a** Extruder motor speed, **b** layer height, **c** overlap percent, and **d** nozzle size

findings recommending reduced layer height to mitigate stair-stepping effects [23]. Nozzle size follows, contributing around 20%, and the squared power of extruder motor speed [ω^2] contributes approximately 10%. Referring to Fig. 16b for valleys and ridges, extruder motor speed holds the most significant influence at 38%, followed by the squared power of overlap percent [p^2] at 18%, the interaction between layer height and overlap percent at 16%, and layer height at 14%.

The response optimizer tool in Minitab was used to determine optimal printing parameters with the model response fit of 0.694 mm for stair-stepping depth and 0.762 mm for valleys and ridges, as shown in Table 4. For the validation, three specimens were fabricated at optimized parameters and the stair-stepping and valleys and ridges showed 3.12% and 0.26% deviation from the model response. The standard deviation for both observed

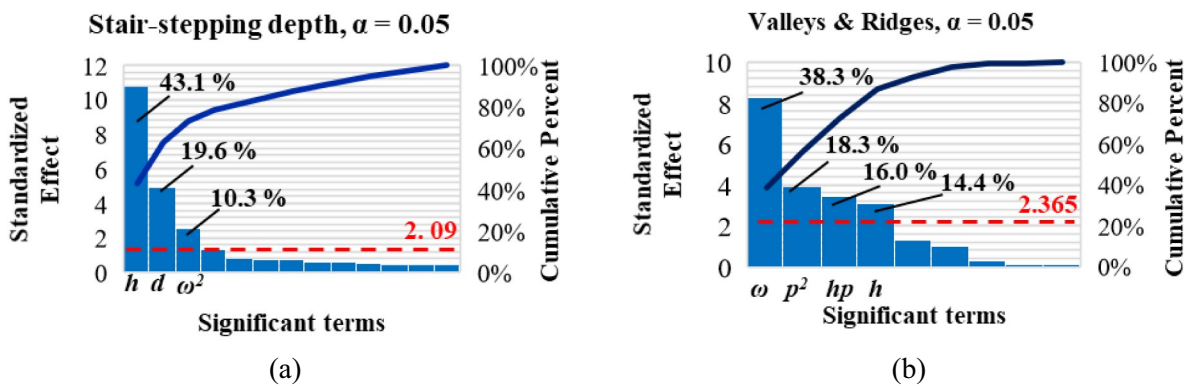
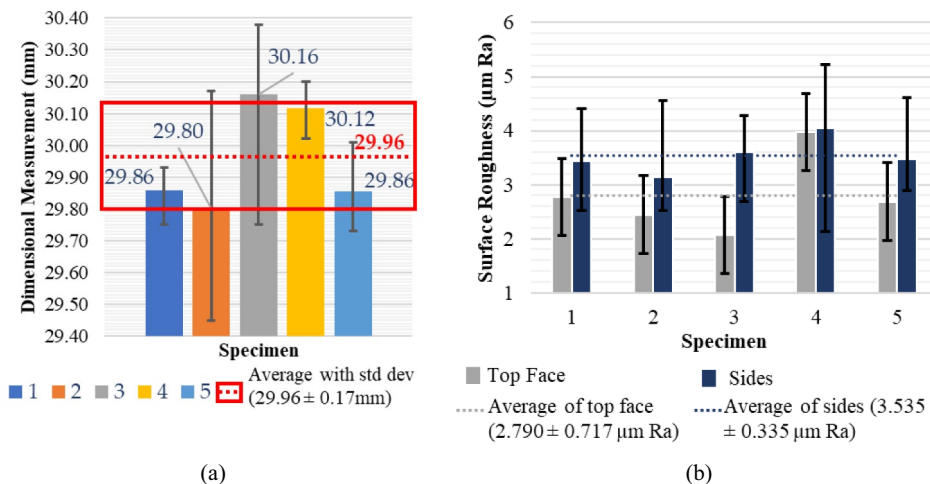


Fig. 16 Pareto chart of influential parameters on response variables: (a) stair-stepping depth and (b) valleys and ridges

Table 4 Optimal printing parameters and model validation

Independent variables	Extruder motor speed (ω , RPM)	Layer height (h , mm)	Overlap percent (p , %)	Nozzle size (d , mm)
Optimal value	420	2.0	2.8	4
Model validation				
Response type	Model response fit (mm)	Average observed response (mm)	Percent deviation (%)	95% CI
Stair-stepping depth	0.694	0.673 ± 0.011	3.12	(0.597, 0.791)
Valleys & Ridges	0.762	0.760 ± 0.056	0.26	(0.543, 0.982)

Fig. 17 a Dimensional tolerance, and b Surface roughness of the processed cuboidal specimens



responses is within the 95% confidence interval, substantiating the model's validity.

3.3 Dimensional tolerance and surface roughness

Five cuboids were printed at optimal parameters and machined through the developed hybrid system to evaluate the dimensional tolerance and surface roughness, and

the results are plotted in Fig. 17. For the dimensional tolerance, with a target measurement of 30 mm, each specimen was measured five times in breadth and length, and their mean and standard deviations were calculated and plotted in Fig. 17a. The average reading for all five specimens was 29.96 mm, resulting in an average error of 40 microns. The standard deviation was 170 microns, falling within acceptable IC limits of 50–254 microns [10]. Similarly, the

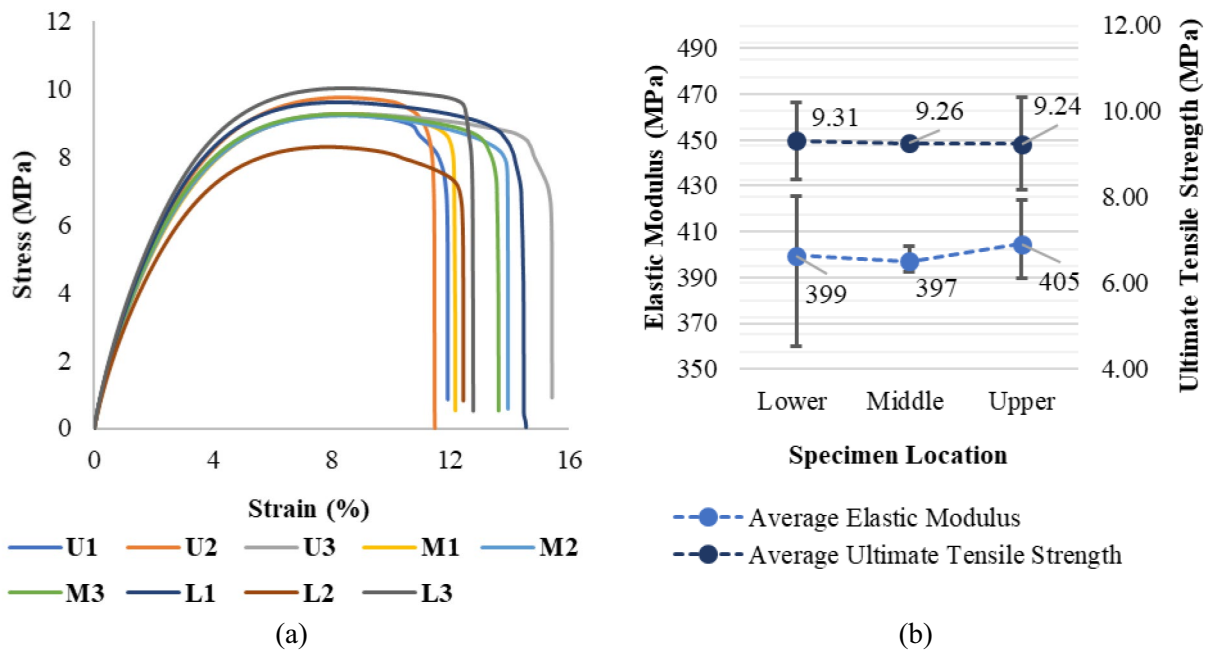


Fig. 18 a Stress–strain plots and b mechanical characterization of wax dog-bone specimens

surface roughness of each specimen was measured multiple times at the top and sides, with mean and standard deviation plotted in Fig. 17b. The plot indicates slightly lower surface roughness on the top face than the sides, likely due to different end milling operations, face milling compared to shoulder milling, respectively. The average surface roughness for the top face was $2.790 \pm 0.717 \mu\text{m Ra}$ and $3.535 \pm 0.335 \mu\text{m Ra}$ for the sides. Both values surpass the $16\text{--}20 \mu\text{m Ra}$ IC range [10], demonstrating geometric compatibility for fabricating wax sacrificial patterns for investment casting.

3.4 Tensile testing and cavity characterization

Tensile tests were performed on nine longitudinal dog-bone specimens extracted from three plates at different vertical heights to assess its potential influence on the material strength due to microstructural changes. Figure 18a shows stress–strain curves for all specimens. The first character of the legend indicates specimen location (upper, middle, or lower), and the second denotes the plate number. Analysis of stress–strain plots revealed consistent mechanical behavior and strength across all plate locations.

Young's modulus and ultimate tensile strength were determined following ISO 527 guidelines [33], using the regression method for Young's modulus and considering the maximum stress for ultimate tensile strength. Figure 18b shows that upper location specimens exhibited the highest average elastic modulus ($405 \pm 18 \text{ MPa}$), followed by lower

($399 \pm 35 \text{ MPa}$) and middle ($397 \pm 6 \text{ MPa}$). For ultimate tensile strength, the maximum average strength was observed in the lower location specimen ($9.31 \pm 0.9 \text{ MPa}$), followed by the middle ($9.26 \pm 0.02 \text{ MPa}$) and upper ($9.24 \pm 1 \text{ MPa}$). One-way ANOVA ($\alpha=0.05$) [30] revealed no significant difference in mean values among different locations for modulus and strength (p values of 0.92 and 0.341, respectively). This supports the null hypothesis that all means are equal. Therefore, the overall average modulus for the longitudinally 3D-printed wax specimen was $400 \pm 20 \text{ MPa}$, and the overall average tensile strength is $8.9 \pm 1 \text{ MPa}$, consistent with the findings of Yusof [35].

Porosity in 3D-printed plates was assessed by machining small cubes at random locations (Fig. 11). Figure 19a shows the cube weight and volume details that were used to compute density. This density was normalized by the wax density, yielding relative density. Porosity percentage is obtained by subtracting relative density from 100 and is presented in Fig. 19b. The average porosity in the cubes was $0.52\% \pm 0.1\%$, indicating the machine's capability to produce objects with total density.

3.5 Case study: fabrication of ASME slip-on flange

To assess the industrial and manufacturing capabilities of the developed hybrid manufacturing system (Fig. 4), a $1\frac{1}{2}$ inch slip-on flange was printed using wax, following optimal parameters, and subsequently machined, as shown in Fig. 20. Dimensional tolerance and surface roughness were

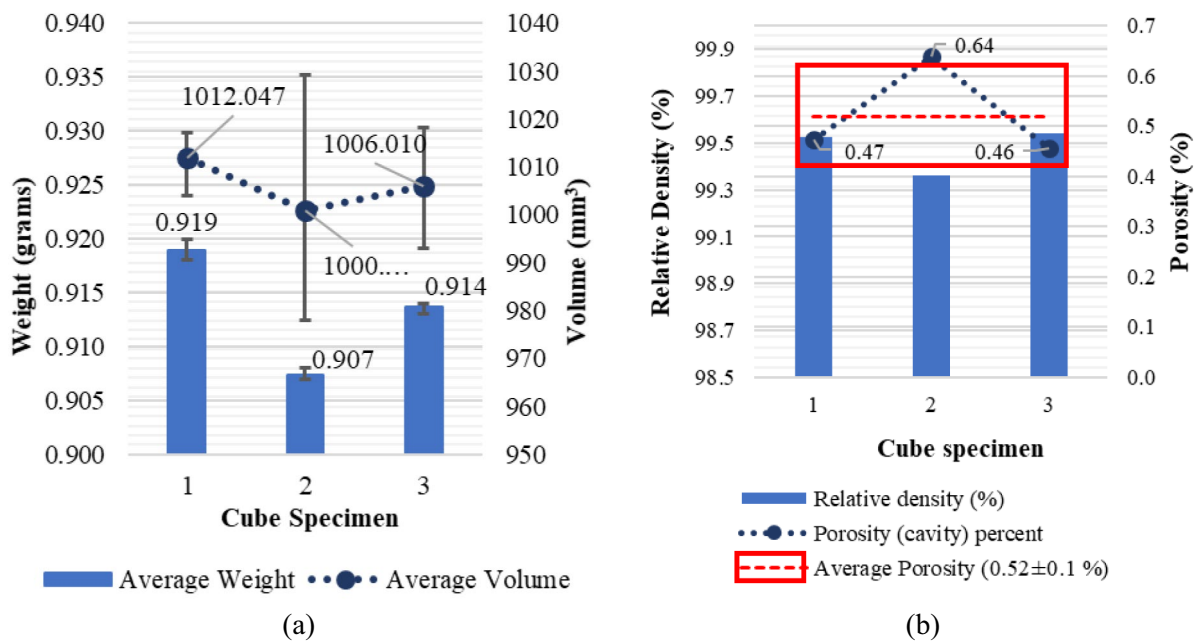


Fig. 19 a Weight and volume of, and b relative density and porosity observed in the machined and 3D printed cubes

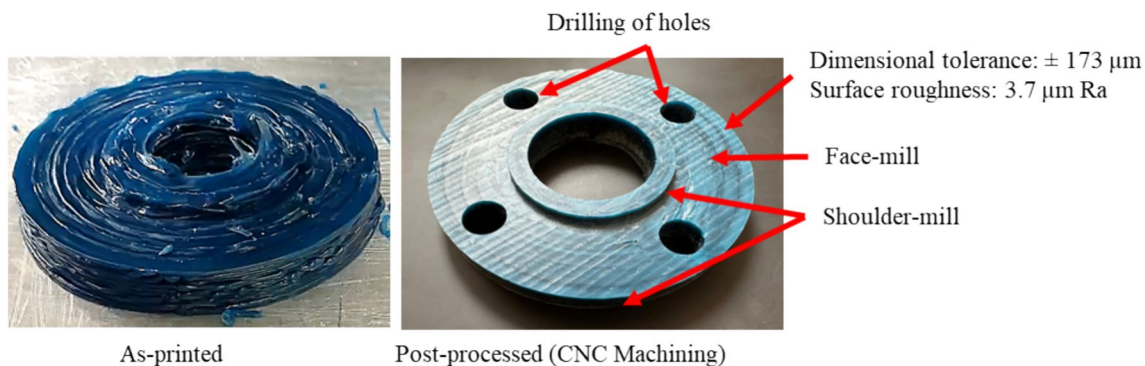


Fig. 20 Case study on the ASME B16.5 Class 150# wax flange fabrication

Table 5 Time taken to fabricate the same flange with different 3D printers

3D Printing type and model	Pre-processing software	Layer height (mm)	Material	Printing time	Post-processing time	Total fabrication time
FDM Ender 5	Ultimaker Cura	0.2	PLA	19 h. 48 min	40 min	20 h. 28 min
FDM MakerBot	Ultimaker Cura	0.15	PLA	30 h. 32 min	40 min	31 h. 10 min
FDM Prusa i3	Ultimaker Cura	0.15	PLA	30 h. 32 min	40 min	31 h. 10 min
SLA Form 2	Perform	0.05	Castable wax	13 h. 30 min	70 min	14 h. 40 min
FGF in-house hybrid system	Elementiam Element X	2.0	Wax pellets	35 min	30 min	65 min

measured to verify compliance with acceptable limits for IC applications. The 3D scan revealed an average volumetric dimensional deviation of $\pm 170 \mu\text{m}$ and a surface roughness

of $3.7 \mu\text{m Ra}$. These values align with those obtained during the experimentation on cubes and fall within the acceptable range for IC applications. The printing process took 35 min,

with an additional 30 min for post-processing (machining). In contrast, the time required to produce the same size flange with 100% infill through a conventional desktop FDM and SLA printers is measured through the preprocessing software and showcased in Table 5, where a substantial reduction in lead time (10–20 times higher productivity) was noticed with the proposed hybrid manufacturing system, showcasing its effectiveness in producing intricate and precise components for industrial use.

4 Conclusion

In summary, this study introduces a novel approach to advance rapid investment casting processes through the integration of large-scale extrusion-based FGF-AM technology with CNC machining. By addressing existing challenges related to scalability, material selection, and surface quality, the developed hybrid manufacturing system presents a promising avenue for improving productivity and quality in industrial settings. The utilization of wax as a sacrificial pattern material and the optimization of printing parameters contribute to minimizing printing defects while ensuring structural integrity and considering sustainable development by using recycled materials. The incorporation of in-situ CNC machining module enhances surface quality, achieving required dimensional accuracy that aligns with investment casting standards. The obtained results demonstrate satisfactory performance metrics, including optimal extruder throughput, mechanical properties of printed wax, and low porosity of the final product, thereby validating the system's capability to produce dense patterns. The successful fabrication of an ASME wax slip-on flange in an industrial-scale case study underscores the practical applicability and scalability of the hybrid manufacturing system.

In future, the research will focus on enhancing the system's capabilities by integrating a large-scale investment shell production module and implementing in-situ quality control through non-contact metrology techniques. These advancements hold promise for further reducing total cycle time and enhancing overall efficiency of the process.

Acknowledgements This research is supported by research grants from Alberta Innovates and Natural Sciences and Engineering Research Council of Canada.

Declarations

Conflict of interest On behalf of all the authors, the corresponding author states that there is no conflict of interest.

References

1. Badanova N, Perveen A, Talamona D (2022) Study of SLA printing parameters affecting the dimensional accuracy of the pattern and casting in rapid investment casting. *J Manuf Mater Process* 6:109. <https://doi.org/10.3390/JMMP6050109>
2. Badanova N, Perveen A, Talamona D (2021) Concise review on pattern making process in rapid investment casting: technology, materials & numerical modelling aspect. *Adv Mater Process Technol* 8:966–978. <https://doi.org/10.1080/2374068X.2021.1959113>
3. Investment Casting Market Size, Share, Growth, Analysis, 2023–2028, (n.d.). <https://www.imarcgroup.com/investment-casting-market> (Accessed 8 July 2023)
4. Cheah CM, Chua CK, Lee CW, Feng C, Totong K, Lee CW, Totong K (2004) Rapid prototyping and tooling techniques: a review of applications for rapid investment casting. *Int J Adv Manuf Technol*. <https://doi.org/10.1007/s00170-003-1840-6>
5. Chua CK, Feng C, Lee CW, Ang GQ (2005) Rapid investment casting: direct and indirect approaches via model maker II. *Int J Adv Manuf Technol* 25:26–32. <https://doi.org/10.1007/S00170-004-1865-5/METRICS>
6. Morsiya CV, Pandya SN (2022) Recent advancements in hybrid investment casting process—a review. *Lect Notes Mech Eng*. https://doi.org/10.1007/978-981-16-7787-8_65/FIGURES/2
7. Kumar P, Ahuja IS, Singh R (2016) Effect of process parameters on surface roughness of hybrid investment casting. *Progress Addit Manuf* 1:45–53. <https://doi.org/10.1007/S40964-016-0004-9/TABLES/6>
8. Wong KV, Hernandez A (2012) A review of additive manufacturing. *Int Sch Res Netw ISRN Mech Eng*. <https://doi.org/10.5402/2012/208760>
9. A. Kaushik, U. Punia, S. Gahletia, R.K. Garg, D. Chhabra (2023) Identification and overcoming key challenges in the 3D printing revolution. *3D Printing and Sustainable Product Development* 87–104. <https://doi.org/10.1201/9781003306238-5/IDENTIFICATION-OVERCOMING-KEY-CHALLENGES-3D-PRINTING-REVOLUTION-ASHISH-KAUSHIK-UPENDER-PUNIA-SUMIT-GAHLETIA-RAMESH-KUMAR-GARG-DEEPAK-CHHABRA>
10. Lee CW, Chua CK, Cheah CM, Tan LH, Feng C (2004) Rapid investment casting: Direct and indirect approaches via fused deposition modelling. *Int J Adv Manuf Technol* 23:93–101. <https://doi.org/10.1007/S00170-003-1694-Y/TABLES/7>
11. Tiwary VK, Arunkumar P, Deshpande AS, Rangaswamy N (2019) Surface enhancement of FDM patterns to be used in rapid investment casting for making medical implants. *Rapid Prototyp J* 25:904–914. <https://doi.org/10.1108/RPJ-07-2018-0176/FULL/PDF>
12. Mfm O, Sharif S, Busari M (2012) Evaluation of direct rapid prototyping pattern for investment casting. *Adv Mater Res*. <https://doi.org/10.4028/www.scientific.net/AMR.463-464.226>
13. Liu Q, Sui G, Leu MC (2002) Experimental study on the ice pattern fabrication for the investment casting by rapid freeze prototyping (RFP). *Comput Ind* 48:181–197. [https://doi.org/10.1016/S0166-3615\(02\)00042-8](https://doi.org/10.1016/S0166-3615(02)00042-8)
14. Yodice A (2000) The freeze cast process. *SAE Techn Pap*. <https://doi.org/10.4271/2000-01-1384>
15. Polzin C, Spath S, Seitz H (2013) Characterization and evaluation of a PMMA-based 3D printing process. *Rapid Prototyp J* 19:37–43. <https://doi.org/10.1108/13552541311292718>
16. Dotchev KD, Dimov SS, Pham DT, Ivanov AI (2007) Accuracy issues in rapid manufacturing CastForm™ patterns. *Proc Inst*

- Mech Eng B J Eng Manuf 221:53–67. <https://doi.org/10.1243/09544054JEM676>
17. Nigam A, Tai BL (2021) Investigation of in-situ surface polishing for fused filament fabrication, ASME 2020 15th international manufacturing science and engineering conference. MSEC 2020:1. <https://doi.org/10.1115/MSEC2020-8445>
 18. Singh S, Kumar P, Singh J (2021) An approach to eliminate shell cracking problem in fused deposition modeling pattern based investment casting process. IOP Conf Ser Mater Sci Eng 1091:012035. <https://doi.org/10.1088/1757-899X/1091/1/012035>
 19. Yao WL, Leu MC (1999) Analysis of shell cracking in investment casting with laser stereolithography patterns. Rapid Prototyp J 5:12–20. <https://doi.org/10.1108/13552549910251837/FULL/PDF>
 20. Kumar P, Ahuja IPS, Singh R (2012) Application of fusion deposition modelling for rapid investment casting—a review. Int J Mater Eng Innov 3:204–227. <https://doi.org/10.1504/IJMATEI.2012.049254>
 21. Justino Netto JM, Idogava HT, Frezzatto Santos LE, Silveira ZC, Romio P, Alves JL (2021) Screw-assisted 3D printing with granulated materials: a systematic review. Int J Adv Manuf Technol 115:2711–2727. <https://doi.org/10.1007/S00170-021-07365-Z/FIGURES/11>
 22. Vicente CMS, Sardinha M, Reis L, Ribeiro A, Leite M (2023) Large-format additive manufacturing of polymer extrusion-based deposition systems: review and applications. Progress Addit Manuf. <https://doi.org/10.1007/S40964-023-00397-9>
 23. Wang F, Bian H, Wang F, Rosenblum E, Garaud P, Traxler A, Mishra A, Srivastava V, Kumar Gupta N, Dharma Bintara R, Zakariya Lubis D, Rohmat Aji Pradana Y (2021) The effect of layer height on the surface roughness in 3D Printed Polylactic Acid (PLA) using FDM 3D printing. IOP Conf Ser Mater Sci Eng 1034:012096. <https://doi.org/10.1088/1757-899X/1034/1/012096>
 24. Tomal ANMA, Saleh T, Khan MdR (2018) Combining fused deposition modelling with abrasive milling to attain higher dimensional accuracy and better surface finish on the finished product. IIUM Eng J 19:221–231. <https://doi.org/10.31436/iiumej.v19i2.960>
 25. Top Applications of Investment Casting - CFS Foundry, (n.d.). <https://www.investmentcastchina.com/investment-casting-applications/> (Accessed 1 May 2024)
 26. Desktop SJ35 extruder, pelletizer, granulating line - RobotDigg, (n.d.). <https://robotdigg.com/product/1752/Desktop-SJ35-extruder,-pelletizer,-granulating-line> (Accessed 16 Nov 2023)
 27. 3D Printing Wax - MachinableWax.com, (n.d.). <https://machinablewax.com/3d-printing-wax/> (Accessed 16 Nov 2023)
 28. Hu F, Mikolajczyk T, Pimenov DY, Gupta MK (2021) Extrusion-based 3D printing of ceramic pastes: mathematical modeling and in situ shaping retention approach. Materials 14:1137. <https://doi.org/10.3390/MA14051137>
 29. PRO2-P100B25A1 - Profiler | SICK, (n.d.). <https://www.sick.com/at/en/catalog/products/distance-sensors/distance-sensors/profiler/pro2-p100b25a1/p/p356646> (Accessed 16 Nov 2023)
 30. ANOVA: Complete guide to Statistical Analysis & Applications, (n.d.). <https://www.analyticsvidhya.com/blog/2018/01/anova-analysis-of-variance/> (Accessed 13 Feb 2024)
 31. Data Analysis, Statistical & Process Improvement Tools | Minitab, (n.d.). <https://www.minitab.com/en-us/> (Accessed 16 Nov 2023)
 32. Confocal Laser Scanning Microscopes, (n.d.). https://www.zeiss.com/microscopy/en/products/light-microscopes/confocal-microscopes.html?utm_source=google&utm_medium=cpm&utm_campaign=C-00008044&gad_source=1&gclid=CjwKCAiAu9yqBhBmEiwAHTx5p0apn9AJXvjxaAYD6nho20qauhCMZj9FMpVNTQoM9gEsyCE7R9w0RoClnYQAvD_BwE#lsm (Accessed 16 Nov 2023)
 33. ISO - ISO 527–2:2012 - Plastics—Determination of tensile properties—Part 2: Test conditions for moulding and extrusion plastics, (n.d.). <https://www.iso.org/standard/56046.html> (Accessed 15 May 2022)
 34. Out of Production 3300 Series Universal Testing Systems | Instron, (n.d.). <https://www.instron.com/en/products/testing-systems/universal-testing-systems/low-force-universal-testing-systems/3300-series> (Accessed 16 Nov 2023)
 35. M.Y. Zaley, (2013) Mechanical Properties Study of Recycled Machinable Wax

Publisher's Note Springer Nature remains neutral with regard to jurisdictional claims in published maps and institutional affiliations.

Springer Nature or its licensor (e.g. a society or other partner) holds exclusive rights to this article under a publishing agreement with the author(s) or other rightsholder(s); author self-archiving of the accepted manuscript version of this article is solely governed by the terms of such publishing agreement and applicable law.